RSC Advances

This is an *Accepted Manuscript*, which has been through the Royal Society of Chemistry peer review process and has been accepted for publication.

Accepted Manuscripts are published online shortly after acceptance, before technical editing, formatting and proof reading. Using this free service, authors can make their results available to the community, in citable form, before we publish the edited article. This *Accepted Manuscript* will be replaced by the edited, formatted and paginated article as soon as this is available.

You can find more information about *Accepted Manuscripts* in the Information for Authors.

Please note that technical editing may introduce minor changes to the text and/or graphics, which may alter content. The journal's standard Terms & Conditions and the Ethical guidelines still apply. In no event shall the Royal Society of Chemistry be held responsible for any errors or omissions in this *Accepted Manuscript* or any consequences arising from the use of any information it contains.

ROYAL SOCIETY OF CHEMISTRY

www.rsc.org/advances

Well Dispersed Silicon Nanospheres Synthesized by RF Thermal Plasma and Their High Thermal Conductivity and Dielectric Constant in Polymer Nanocomposites

Guolin Hou[a, b‡], Benli Cheng[c‡], Fei Ding[a], Mingshui Yao[d], Yuebin Cao[a], Peng Hu[a], Ruixin Ma[c], and Fangli Yuan[a,*]

[a] State Key Laboratory of Multi-phase Complex Systems, Institute of Process Engineering, Chinese Academy of Sciences (CAS), China

[b] University of Chinese Academy of Sciences (UCAS), No.19A Yuquan Road, Beijing 100049, China

[c] School of Metallurgical and Ecological Engineering, University of Science and Technology Beijing, Beijing 100083, China

[d] State Key Laboratory of Structural Chemistry, Fujian Institute of Research on the Structure of Matter, Chinese Academy of Sciences (CAS), 155 Yangqiao Road west, Fuzhou, 350002, China

[*]Corresponding author. E-mail: flyuan@home.ipe.ac.cn; Fax: +86-10-62561822; Tel: +86-10-82544974

Abstract

In this paper, well dispersed Si nanospheres (Si-NSs) were successfully synthesized via a simple and efficient method by using radio-frequency (RF) thermal plasma. Structures and morphologies of the prepared samples were characterized by various techniques, including XRD, EDX, FESEM, HRTEM, SAED, BET and Raman spectroscopy. It is found that the obtained Si-NSs present uniform spherical shape,

RSC Advances Accepted Manuscript

smooth surface. The effects of experimental parameters (including quenching gas and length of reaction path) on morphology and size distribution of Si particles were investigated. The growth mechanism of Si nanoparticles in the thermal plasma was discussed. Si-NS/phenolic resin (PR) composites were fabricated and their performances including thermal stability, thermal conductivity, and dielectric properties were measured. It indicates the composites exhibit high thermal conductivity (6.2 W m^{-1} K^{-1}) and dielectric constants of 106 at 100 Hz, which implies they are applicable for energy storage-capacitors. The high thermal conductivity and dielectric constant can be attributed to their uniform spherical shape and smooth surface, which enable them disperse uniformly in the polymer matrix.

1 Introduction

Organic–inorganic composites with selected functional components exhibit superior properties to that of their parent materials, and show wide applications such as photovoltaic (PV) devices, microelectronics, lithium-ion battery and capacitors.[1-4] A typical example is polymer–inorganic composites with high thermal conductivity and large dielectric constant, which are highly desirable to meet the requirement of heat dissipation and capacitive density for energy-storage device.[5,6] Plenty of work targeting to improve the dielectric constant of polymers has been developed. Conductive materials such as carbon nanofibers (CNF),[7] multiwall carbon nanotube (MWCNT)[8-11] and graphene-encapsulated carbon nanotube (G-CNT)[12] are used as fillers incorporated into polymer matrix to improve the dielectric constant, however, the dielectric loss also remarkably jumps up and the breakdown strength heavily drops

RSC Advances Accepted Manuscript

down, which greatly restricts their practical applications. Recently, ferroelectric ceramics with high dielectric constant ($BaTiO_3$, $BaSr_xTiO_3$)[13,14] have been introduced in the polymer matrix and acquire relatively high dielectric constant. However, they still can't get rid of the adverse effect on the breakdown strength of composites. Except for dielectric constant, thermal conductivity of the dielectric materials is also very disirable for the heat dissipation in dielectric composites, but few work has been focused on it. Lee reported that the thermal conductivity could be increased to 2.42 W m^{-1} K^{-1} for epoxy resin filled with AlN at its maximum loading of 60 vol.%.[15] By adding SiC whiskers with its maximum loading of 20.0 vol %, Li increased the thermal conductivity of PVDF to 0.6 W m^{-1} K^{-1}.[16] Although great effort has been made, the effect is moderate. Therefore, it remains a challenging task to improve the thermal conductivity and dielectric constant at the same time, without significant reduce of dielectric breakdown strength and abrupt increase of dielectric loss. As a semiconductor, silicon shows great potential on photovoltaic devices and microelectronics due to its relatively high thermal conductivity (up to 148 W m^{-1} K^{-1}) and excellent dielectric property (the dielectric constant is 11.9). However, for irregular micron particles, the improvement is limited even at high filler content due to the difficulties in achieving homogeneous dispersion and forming efficient thermal conductive paths in composite.[17] It had been realized nano-sized spherical particles with smooth surface, which are apt to be uniformly dispersed in polymer, would be beneficial to form thermal conductive networks and thus obtain relatively high thermal conductivity.[18] In fact, the improvement of the fillers' dispersion in host

RSC Advances Accepted Manuscript

polymer is also an effective way to lower percolation threshold and achieve large dielectric constant.[19] Considering from the above two aspects of high thermal conductivity and large dielectric constant, nano-sized silicon particles with spherical shape and homogeneous dispersion in polymer matrix are highly desired for the composites' practical application in energy storage capacitors.

During the past few years, a variety of chemical and physical methods have been employed to fabricate silicon nanoparticles.[20-25] However, these techniques are restricted by kinds of drawbacks such as high-cost, low yield, and hard to control particle size and morphology, which limit their further applications. Inductively coupled radio-frequency (RF) thermal plasma vaporization route may be attractive for overcoming the above limitations. Two of the great advantages of RF thermal plasma are high reaction temperature (up to 10^4 K) and steep cooling rate (10^5-10^6 K s^{-1}). In addition, adjustable operation parameters make it possible to control the particle size, phase and morphology, and sustainable operation makes it possible in large-scale production. Moreover, compared with direct-current (DC) plasma, it is especially suitable for synthesizing materials with high purity, which is vitally important for microelectronics device. By controlling thermodynamic and kinetic factors, nanomaterials with various morphologies and sizes have been successfully synthesized in our previous work.[26-29]

In this work, large-scale of Si-NSs were prepared in RF thermal plasma system at atmospheric pressure. The significant features of the prepared Si-NSs are their nearly perfect spherical shape, narrow size distribution and well dispersity. Operation

RSC Advances Accepted Manuscript

parameters affecting the morphology and size distribution of Si were investigated. At last, the as-prepared Si-NSs were used to prepare Si/PR nanocomposites, and their thermal conductivity and dielectric properties were evaluated. It was found that the Si-NS/PR nanocomposites showed high thermal conductivity and large dielectric constants with enhanced dielectric breakdown strength and low dielectric loss. These results demonstrate their potential application in energy conversion and storage electronic devices with high heat dissipation.

2 Experimental

2.1 Preparation of Si nanoparticles

The experimental apparatus are composed of the following parts: RF induction plasma generator system (used to generate the electromagnetic field); raw material feeder system; products collection system (including heat exchange chamber cooling by water; gas-solid separation chamber); exhaust system; and a gas supply and control system. The schematic illustration of the configuration of the apparatus is available in our published literature.[26]

For Si nanospheres synthesis, the starting powder of large size Si (>99.9%, 5~20 μm) were delivered into plasma by carrier gas in a continuous way. In order to reduce the interference of other factors, the plasma source power input and the frequency were maintained at 10 KW and 4 MHz respectively. When powders went through plasma torch, a series of physical vapor reaction would occur in a very short time. They were rapidly transported into heat exchange chamber and deposited on chamber after cooling. To discuss effects of cooling rate on the products, natural cooling in the

RSC Advances Accepted Manuscript

absence of quenching gas and rapid cooling by injecting transverse quenching gas below the plasma torch were used. The typical operating parameters of plasma are given in Table 1. After reaction, yellowish-brown deposited Si nanoparticles in the plasma reactor chamber were harvested.

Table 1 Thermal plasma operating parameters in Si nanoparticles synthesis

Operating parameters	value
Plasma power input	10 kW
Applied frequency	4 MHz
Flow rate of central gas, argon	0.8 $m^3 h^{-1}$
Flow rate of sheath gas, argon	1 $m^3 h^{-1}$
Flow rate of carrier gas, argon	0.3 $m^3 h^{-1}$
Flow rate of quenching gas, argon	6 $m^3 h^{-1}$
Raw material	5~20 μm
Powder feed rate	2 g min^{-1}

2.2 Preparation of Si/PR nanocomposites

At first, the as-synthesized Si-NSs or micro-sized Si were dispersed in ethanol and ultrasonicated for 30 min to form suspensions. Subsequently the suspensions were added into a certain amount of liquid PR drop by drop under a continuous mechanical stirring at 60 ℃. Then hexamethylenetetramine (HMTA) was added into the above mixture, and was stirred for another 1h, after that the homogeneous suspensions were degassed at 80 ℃ in a vacuum oven for 30 min. Then the mixture was poured into a stainless steel molds, and cured in an oven at 130 ℃ for 2h. After the molds were

RSC Advances Accepted Manuscript

cooled naturally to room temperature, the Si-NS/PR composites were obtained after demoulding.

2.3 Characterization and Measurement

The phase and crystal structure of obtained products were characterized by X-ray diffraction (XRD, Philips X' Pert PRO MPD) operated at 40 kV and 30 mA with Cu Kα radiation. The morphologies of the samples were observed by field-emission scanning electron microscopy (FESEM, JSM-7001F, JEOL, Tokyo, Japan) and transmission electron microscopy (TEM, JEM-2100, JEOL, Tokyo, Japan). Elemental analysis was determined by energy dispersive X-ray (EDX) attached to the FESEM instrument. X-ray photoelectron spectroscopy (XPS) was conducted to analyze the surface chemical state by a Thermo Scientific ESCALAB 250 Xi XPS system. Raman spectroscopy was performed on Renishaw invia Raman Microscope with an excitation wavelength of 632.8 nm. The Brunauer–Emmett–Teller (BET) surface area of the sample was measured by Micrometrics ASAP 2010 analyzer. Thermal gravimetric analyses (TGA) and Differential scanning calorimetry (DSC) of Si/PR composites were performed with a TG-209 F3 instrument (NETZSCH, Germany) at a heating rate of 10 ℃ min^{-1} under the nitrogen atmosphere. Thermal conductivities of the composites were measured with LFA 427 Nanoflash (NETZSCH, Germany) according to ASTM E1461. The dielectric and electrical properties were examined by an Agilent 4294A impedance analyzer in the frequency range of 100 Hz to 10 MHz. Dielectric breakdown strength was conducted using a dc dielectric strength tester (DH, Shanghai Lanpotronics Co., China) at room temperature in a voltage ramp rate of 2 V

RSC Advances Accepted Manuscript

s^{-1} until the breakdown failure of a sudden current increase.

3 Results and Discussions

3.1 Characterization of Si Nanoparticles

The silicon raw materials display irregular shape with wide particle size distribution from several to 20 micrometers as shown in Fig. 1a. After treated by thermal plasma, nano-scale particles were obtained. Under natural cooling, the Si nanoparticles obtained show irregular spherical shape, with non-uniform size, rough surface and bad dispersity (Fig. 1b), which was denoted as irregular Si nanoparticles (Si-INs). However, when given rapid cooling, the Si nanoparticles with uniform size of about 50 nm show perfect spherical shape, smooth surface and good dispersity (Fig. 1c). The results indicate that the rapid cooling rate contributes to the formation of particles with small size, uniformity, high degree of sphericity and good dispersity. In addition, the specific surface area of Si-NSs was measured to be 56.99 m^2 g^{-1}, corresponding to the theoretical calculated value of spherical particles with the diameter of 46 nm, which matched well with the size of Si-NSs observed by SEM.

The detailed structural analyses of Si nanospheres were further performed using TEM analysis in Fig. 1d, which clearly display the uniform spherical shape and good dispersity of obtained products, consistent with SEM observation. HRTEM (Fig. 1e) shows a clean and perfect crystalline structure, indicating the single-crystalline structure of the nanosphere. The measured lattice fringe spacing of Si-NSs is 0.31 nm, corresponding to (111) plane of diamond cubic structure (Fig. 1e). It, together with the corresponding SAED pattern (inset of Fig. 1e) reveals that the Si-NSs are single

RSC Advances Accepted Manuscript

crystal with high crystallinity. The EDS spectroscopy (Fig. 1f) of Si-NSs indicates that Si is the main element, and 2.86 wt.% oxygen is detected in the products.

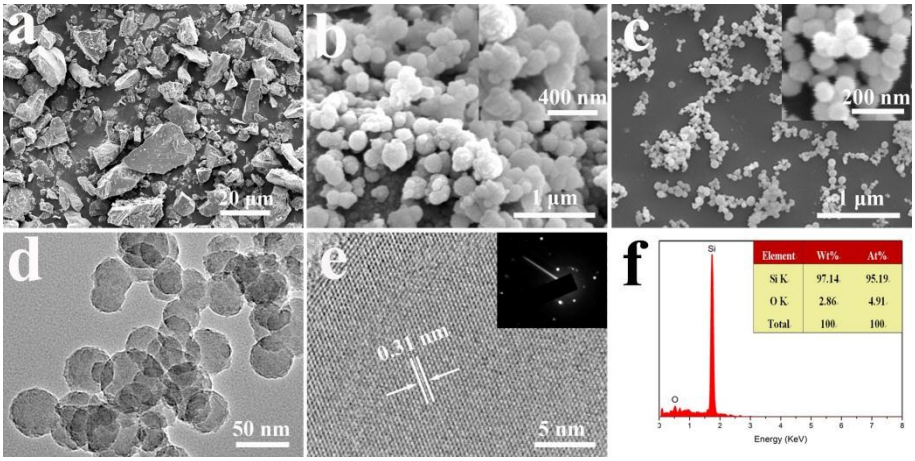

Fig. 1 SEM images of (a) raw Si, (b) Si-INs obtained with natural cooling and (c) Si-NSs obtained with rapid cooling, (d) TEM image of Si-NSs, (e) HRTEM image of Si-NS and the corresponding SAED pattern (inset) and (f) EDS diagram of Si-NSs.

The measurement of XPS was conducted to further confirm the surface/near-surface chemical composition of Si nanospheres. As shown in Fig. 2a, it is mainly composed of Si, O and C elements according to the full-range XPS spectra, of which C contamination is mainly attributed to the residual solvents. More detailed information about the chemical state of these elements can be obtained in the high resolution XPS spectra of the Si 2p and O 1s in Fig. 2b-c. The first peak at lower binding energy (BE, 98.7 eV) is assigned to the unoxidized Si atoms (Si^0) of the Si core, while the second peak at higher BE (103.1 eV) is attributed to fully oxidized Si (Si^{4+} states), in between is suboxide components (Si^{x+} states), forming the Si/SiO_2 interface.[30] In the O 1s spectra, the high BE component located at 532.5 eV is attributed to chemisorbed or dissociated oxygen on the surface of Si nanospheres, such as CO_2 , O_2 or H_2O, while the typical BE (531 eV) of O^{2-} ions for SiO_2 is fair

RSC Advances Accepted Manuscript

weak.[31,32] Therefore, the oxygen in the product is mainly derived from chemisorption and surface oxidation of Si nanospheres when exposed at ambient.

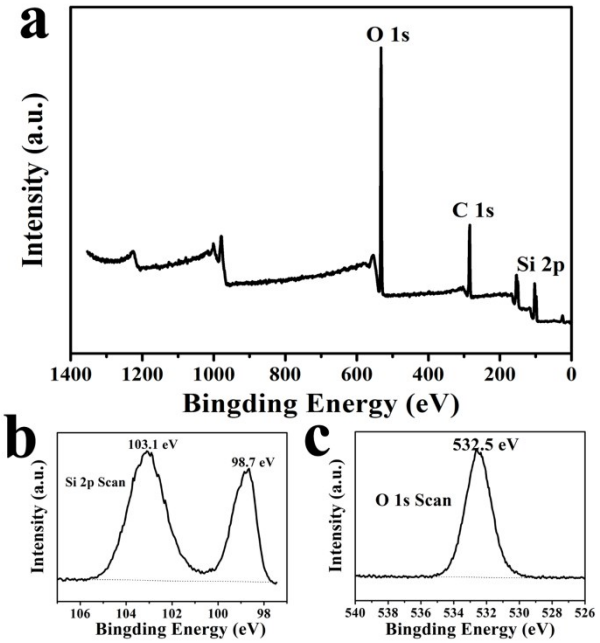

Fig. 2 (a) XPS spectra and (b-c) high resolution XPS spectra of Si nanospheres at binding energies corresponding to Si 2p and O 1s.

Fig. 3a shows the typical XRD pattern of the Si-NSs and Si-INs synthesized by RF thermal plasma. The sharp diffraction peaks in the XRD patterns reveal their good crystallinity. The characteristic peaks (111), (220), (311), (400), (331) and (422) are well agreement with the standard card (JCPDS No. 00-027-1402), which is face centered cubic (fcc) structure, belonging to the space group Fd-3m with lattice constants of a=b=c=5.431 Å. The crystal structures of the obtained Si-NSs and Si-INs were further characterized by Raman scattering spectra, as shown in Fig. 3b. The spectra peaks of Si-INs are located at 517.8 cm^{-1} and 959.6 cm^{-1}, while the spectra peaks of Si-NSs are located at 514.7 cm^{-1} and 955.1 cm^{-1}. It is widely accepted that the sharp peaks in the vicinity of 520 cm^{-1} and the broad band centered at around 960

RSC Advances Accepted Manuscript

cm^{-1} belong to the first-order transverse optical (TO) and two transverse optical (2TO) phonons, respectively.[33] Compared with Si-INs, the Raman spectrum of Si-NSs presents subtle downwards shift and a broadened full width at half maximum of the first-order phonon mode, which could be attributed to phonon confinement effect.[34,35]

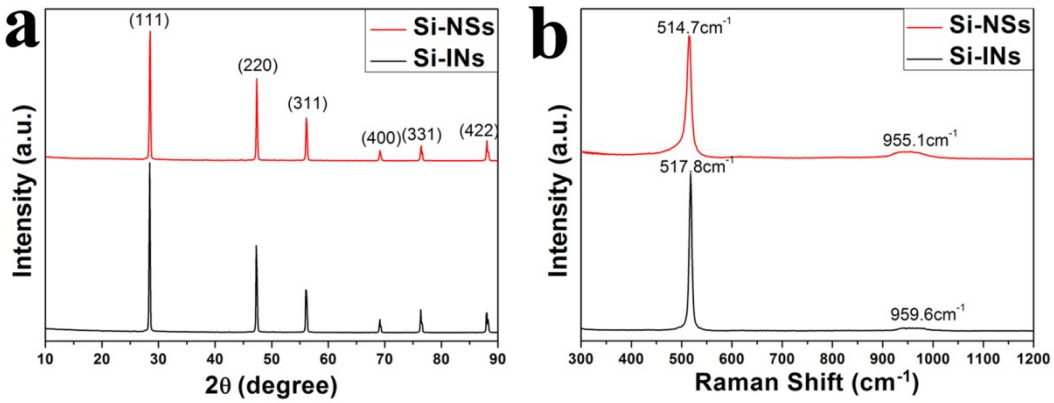

Fig. 3 (a) XRD patterns and (b) Raman spectras of Si-INs and Si-NSs.

Fig. 4a and 4b show the TEM images of Si-NSs deposited on the upper and bottom of reactor wall, respectively. From the images we can see that both of them show spherical shape despite their different deposited location. However, compared to the nano-spheres deposited on the upper part of reactor, the nano-spheres deposited on the bottom exhibit large average diameter and show wide size distribution. Detailed size distributions and diameters of the two kinds of nano-spheres are shown in Fig. 4c. In vapor deposition synthesis process, the residence time plays an important role in the particle size and distribution.[36,37] Compared to the particles deposited on the upper part of reactor, particles deposited on the bottom of reactor have enough time to further nucleate and grow up as they go through longer reaction path. As a result, nanospheres with wider size distribution and larger diameters are finally obtained.[38,39]

RSC Advances Accepted Manuscript

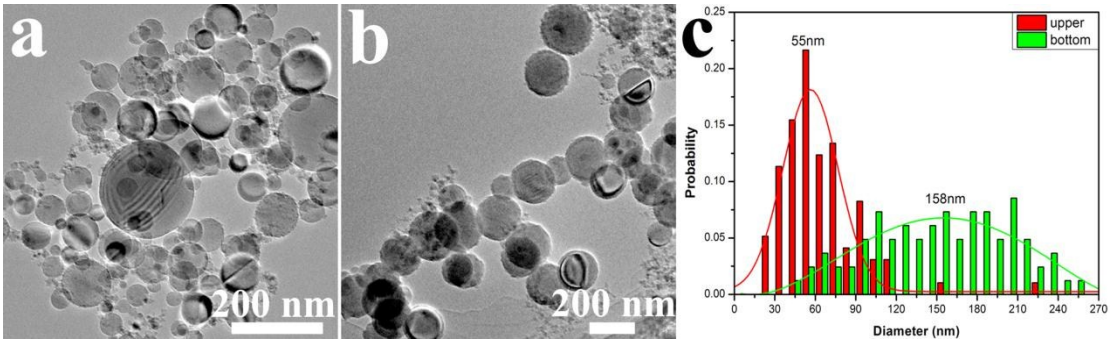

Fig. 4 TEM images of the Si nanospheres deposited on the upper (a) and bottom (b) wall, (c) diameter statistical distribution of the two kinds of Si nanospheres.

3.2 Formation mechanism of Si nanoparticles

In thermal plasma synthesis, it is an intricate heat and mass transfer process that involves phase conversion, interactions among thermo fluid field, electromagnetic field, and particle concentration field.[40-42] To clarify the growth mechanism of Si nanoparticles, the schematic illustration for the formation process was proposed in Fig. 5. At the first stage, irregular micro-sized silicon were melted and evaporated rapidly with the assistance of high enthalpy provided by thermal plasma arc. Subsequently, the vaporized Si transported to the tail of the plasma where the temperature decreased drastically and homogeneously nucleated due to the high degree of supersaturation. Then the Si nuclei get into the crystal growth stage, and at this stage different-shaped Si nanoparticles are obtained due to their different cooling rate. With a natural cooling (i.e. the cooling rate is relatively low), the fresh formed nuclei grew up, agglomerated and formed aggregates, resulting in irregular nanoparticles (Fig. 1b). Whereas, agglomeration can be suppressed at very high temperature gradients for introducing Ar quenching gas.[36] The nanocrystal forming by collision and fusion of nuclei presents spherical shape as it possesses the minimum surface energy (Fig. 1c).[43]

RSC Advances Accepted Manuscript

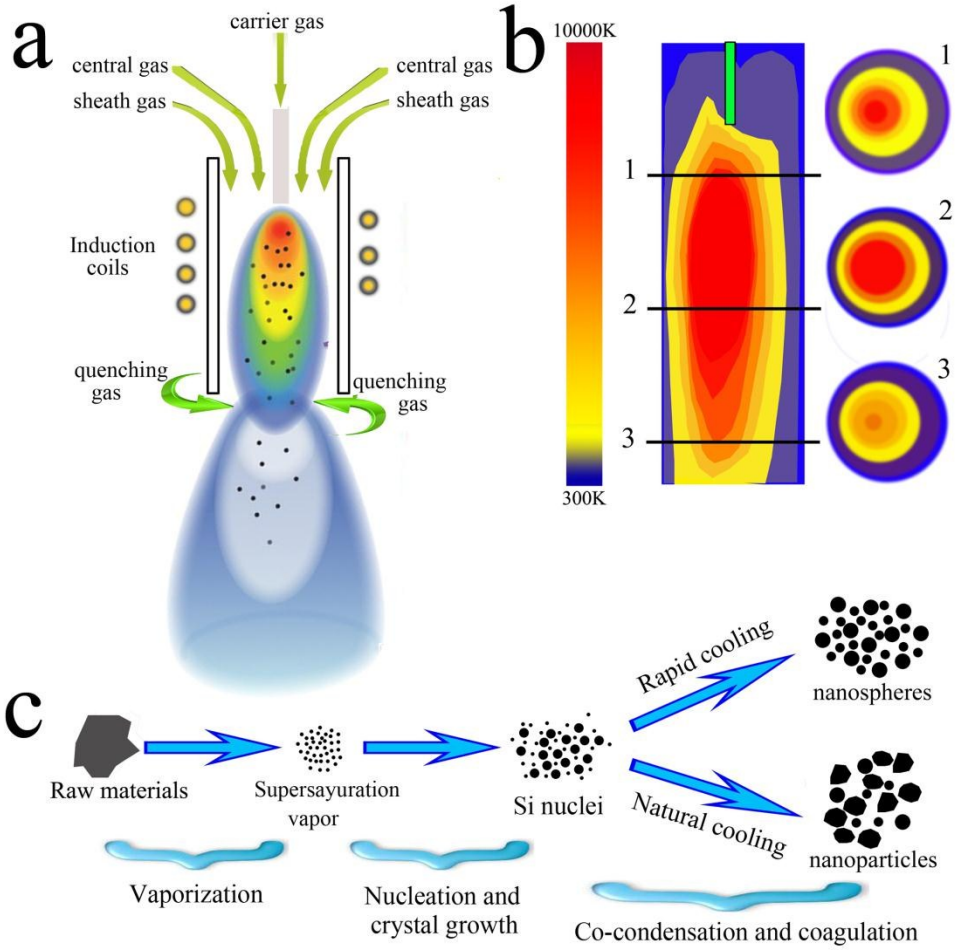

Fig. 5 (a) sketch of the RF plasma reactor, (b) temperature thermofluid field in plasma arc and (c) schematic illustration for silicon nanoparticles growth.

3.3 Thermal stability of Si/PR composites

It has been confirmed that the thermal conductive properties of the polymer nanocomposites are closely associated with the dispersion and interface adhesive between fillers and matrix.[44,45] Therefore, the thermal stability of pure PR and composites were investigated by TG and DSC analysis, respectively. Fig. 6 shows the TG and DTA curves of pure PR and Si-NS/PR composite with 50 wt.% (i.e. 28 vol.%) Si-NS loading. The thermal degradation for both samples can be divided into three stages, which is similar to previous report.[46-48] In the first stage from room

RSC Advances Accepted Manuscript

temperature to 225°C, small terminal groups of the cured resin were removed, accompanied by the formation of additional cross-links as a result of condensation reactions. The second stage for pure PR is from 220 ℃ to 600 ℃, which is corresponding to the decomposition of PR polymer matrix. However, the beginning temperature for PR decomposition in Si-NS/PR is 300 ℃, which is almost 80 ℃ higher than that of pure PR. When the temperature increases to 620 ℃, pure PR was completely decomposed, with 5.1 wt.% char was left. For the Si-NS/PR composite, the weight still shows no change over temperature 620 ℃. However, calculated from the weight loss, it indicates 5.5 wt.% PR was still left in the Si-NS/PR composite. The higher PR decomposition temperature and the existence of PR at high temperature (620-800 ℃) for Si-NS/PR composites indicate PR's thermal stability was improved due to the existence of Si-NSs. This dramatic improvement of thermal stability has a close relationship with the interfacial interaction between nanoparticles and polymer matrix.[49,50] With nanoscale and smooth sphere morphology, Si nanospheres could be dispersed uniformly in the polymer matrix and strong particle/matrix interfacial interaction is introduced, which is an effective way to restrict the thermo motion of polymer chains and improve the thermo stability.[51]

RSC Advances Accepted Manuscript

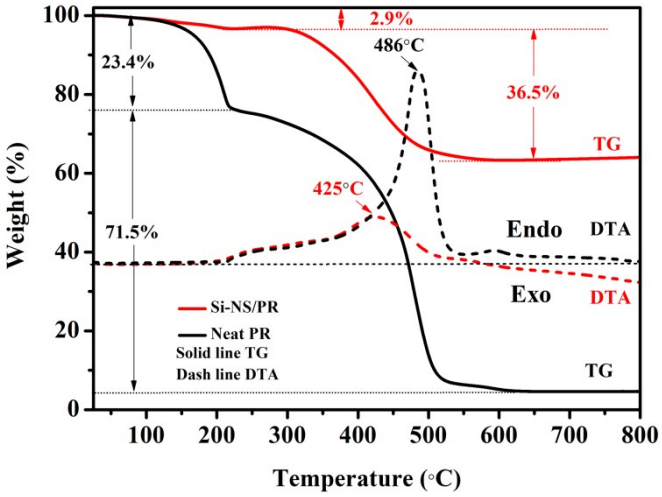

Fig. 6 TG and DTA curves of 50 wt.% Si-NS/PR composite and pure PR under N_2 atmosphere at the heating rate 10 ℃ min^{-1}.

3.4 Thermal conductivity of Si/PR composites

The thermal conductivities of composites incorporated with irregular micron-sized silicon and nano-spherical silicon are presented in Fig. 7. It is obvious that all composites show increased thermal conductivity with the increasement of volume fraction. Both Si-NS/PR and micro-sized-Si/PR composites show moderate thermal conductivities increase at low Si volume fraction and rapidly increase when the filler content is further increased. For example, the thermal conductivity of Si-NS/PR increases from 0.20 to 2.63 W m^{-1} K^{-1}, as the fraction of Si-NSs increases from 0 to 28%. However, when the volume fraction of Si-NSs is over 28 vol%, there is a rapid thermal conductivity increase, and the thermal conductivity of Si-NS/PR is improved to 6.20 W m^{-1} K^{-1} at the volume fraction of 47 vol.%, which is about 30-times higher than the value of pure PR (0.2 W m^{-1} K^{-1}). Importantly, the Si-NS/PR composites exhibit a superior thermal conductivity than micro-sized-Si/PR composites, especially at high filler content. For example, with 47 vol.% filler content,

RSC Advances Accepted Manuscript

the thermal conductivity of Si-NS/PR composite is 6.20 W m^{-1} K^{-1}, almost 2 times of that of micro-sized-Si/PR (the thermal conductivity of micro-sized-Si/PR is only 3.5 W m^{-1} K^{-1} at the filler content of 47 vol.%).

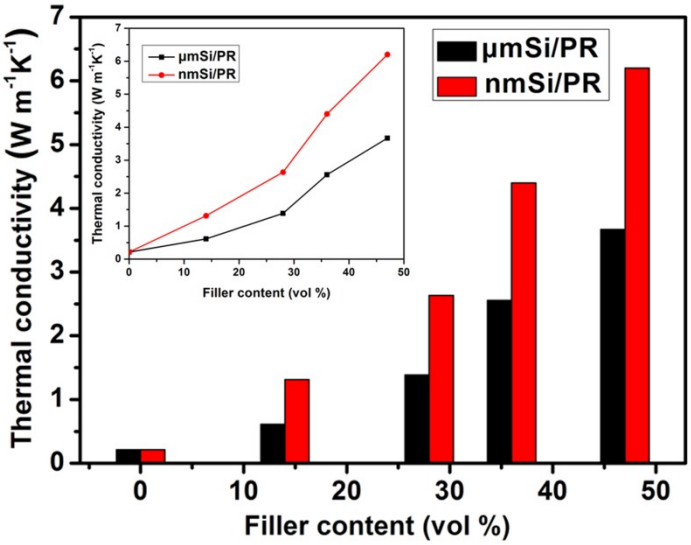

Fig. 7 Thermal conductivities of Si-NS/PR and micro-sized Si/PR composites with different volume fractions of Si.

The typical thermal conductivity change of obtained nano-Si/PR composite could be well explained by the distribution state of nanoparticles in the organic matrix. The SEM images of Si-NS/PR composites with different volume fractions of Si were shown in Fig. 8. At low volume fractions, Si-NSs are isolated like “islands” in matrix, which inhibits the forming of thermal conductive paths and cuts off the diffusion of heat flow, leading to a relative low thermal conductivity. When the filler content reaches to a certain value, thermal conductive paths are formed as the conductive additives interweave with each other. As a result, the resin layer between nanoparticles becomes thinner and the thermal resistance is reduced.[52,53] That is, the thermal conductivity of composite will be mainly dominated by high thermal

RSC Advances Accepted Manuscript

conductive Si (148 W m^{-1} K^{-1}) and increases remarkably. In addition, compared to micron irregular particles and granular aggregate, larger interface would be induced as the Si nanospheres are uniformly dispersed in the polymer matrix. As a result, a strong particle/matrix interfacial interaction is introduced, which has been proved to be an effective way to decrease the interfacial thermal resistance and improve the thermal conductivity.[51,54]

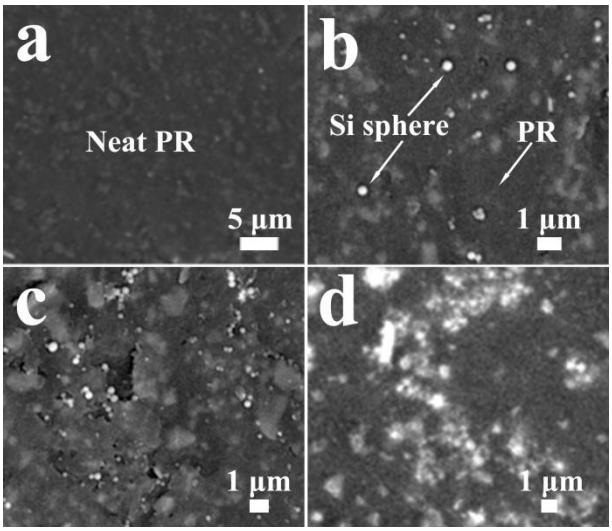

Fig. 8 SEM images of fracture surface of Si-NS/PR with various Si-NSs volume fraction: (a) 0 vol.% (b) 14 vol.% (c) 28 vol.% and (d) 47 vol.%.

3.5 Dielectric properties of Si/PR composites

Fig. 9 shows the frequency dependence of dielectric properties for pure PR and Si-NS/PR composites at different volume fractions of Si-NSs over the frequency range of 10^2 Hz to 10^7 Hz. It can be seen that the dielectric constant ε (Fig. 9a) monotonic increases with the rising of Si-NSs loading and decreases with the frequency increasing. When the filler loading is less than 28 vol.%, ε shows slight variations over the frequency range from 10^2 Hz to 10^7 Hz. However, ε increase rapidly when the filler loading exceeds 36 vol.%, especially at low frequencies part.

RSC Advances Accepted Manuscript

In particular, the dielectric constant ε of composite increases to 106 at 100 Hz with 47 vol.% filler, which is 4 times higher than that of pure PR matrix at the same frequency. The enhancement of ε is mainly ascribed to interfacial polarization which can be explained by the percolation theory.[55] Compared to micron sizes and granular aggregation, large interfacial areas would be induced as the Si nanospheres uniformly dispersed in the polymer matrix. As the electrical conductivity of Si-NSs is quite different from that of polymer matrix, charge carriers of the electrode can migrate and accumulate at the interfaces between Si-NSs and polymer when an electric field is applied on the samples. The migration and accumulation of the charge carriers will lead to a high degree of interfacial polarization, which results in a high dielectric constant.[16] The decrease of ε at high frequencies is caused by the relaxation of PR dipole polarization, that is, orientation polarization of dipoles cannot follow with the external electric field, and thus leads to the decrease of dielectric constant.

The frequency dependence of dielectric loss tangent (tan δ) of Si/PR nanocomposites and pure PR are shown in Fig. 9b. Compared to the pure PR, the tan δ of nanocomposites decreases with the addition of Si-NSs. As we know, there are three aspects causing the dielectric loss:[56,57] conduction (transport-related loss), movement of molecular dipoles (dipolar loss) and space charge (interfacial polarization contribution). It is widely accepted that tan δ is mainly affected by the interfacial polarization at low frequencies, whereas dipolar relaxation process is the dominant factor at high frequencies. At low frequencies, strong interfacial interaction between Si-NSs and PR suppresses the movement of molecular dipoles, resulting in

RSC Advances Accepted Manuscript

low tan δ. At high frequencies, dipole polarization of PR is weakened with the rising of Si-NSs loading (i.e., the content of PR reduced) and leads to a low tan δ. Thus, the dielectric loss tangent tends to remain stable and low value when the packing fraction of Si nanospheres is greater than 36 vol. % in the frequency range of 10^2-10^7 Hz.

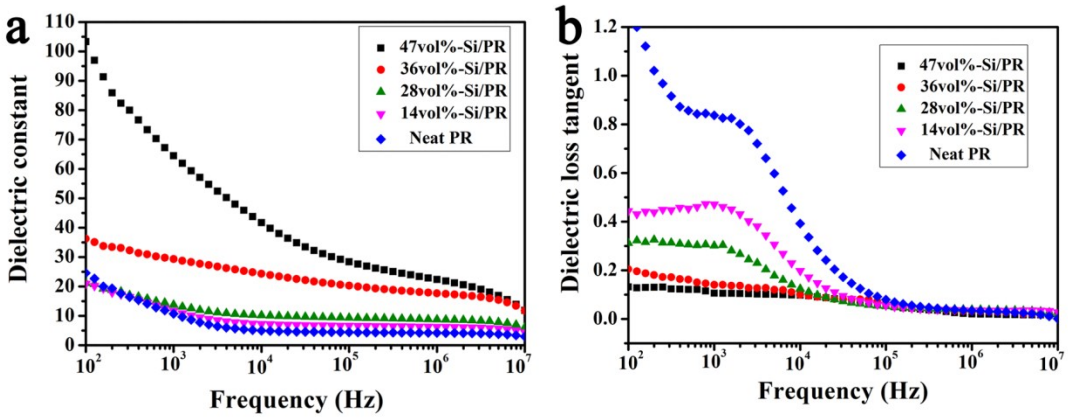

Fig. 9 Frequency dependence of (a) dielectric constant (b) dielectric loss tangent for pure PR and Si-NS/PR composites filled with different Si-NSs contents.

For dielectric material, high dielectric constant is not the only factor in practical applications, high breakdown strength (E_b) is also of great importance, as it determines the operating electric field and the maximum energy storage density of the dielectric material.[58] Normally, particle fillers lead to a decline in the breakdown strength of the polymer matrix, which will hinder the practical application of polymer matrix composites.[13] However, as shown in Fig. 10, the breakdown strength (E_b) of Si/PR nanocomposites increases with a low loading of Si nanospheres. For example, the E_b value of the nanocomposite with 4.1 vol % Si nanospheres increases to 14.2 MV m^{-1}, which represents a 54% increase over the breakdown strength of pure matrix (9.25 MV m^{-1}). With further increasing of the filler loading, The E_b gradually decreases, but is still higher than that of the pure matrix. This interesting phenomenon

RSC Advances Accepted Manuscript

is similar to the result of recent report.[12,59] The E_b increases with a low loading is attributed to the presence of Si nanospheres, which act as scattering centers in the composites and effectively increase the charge scattering, resulting in an increase of breakdown strength.[60,61] However, at high loadings, electrical pathways would formed and enhance the electric field near the interface, due to the differences of electric properties between fillers and polymer, which leads to the E_b of composites gradually decreases.[62] However, it should be note that even at a high filler content of 28 vol %, the E_b value of the nanocomposite is 9.30 MV m^{-1}, which is still slightly higher than that of pure polymer matrix. This is attributed to the uniform dispersion in the polymer matrix and the strong particle/matrix interfacial interaction at such high filler content.

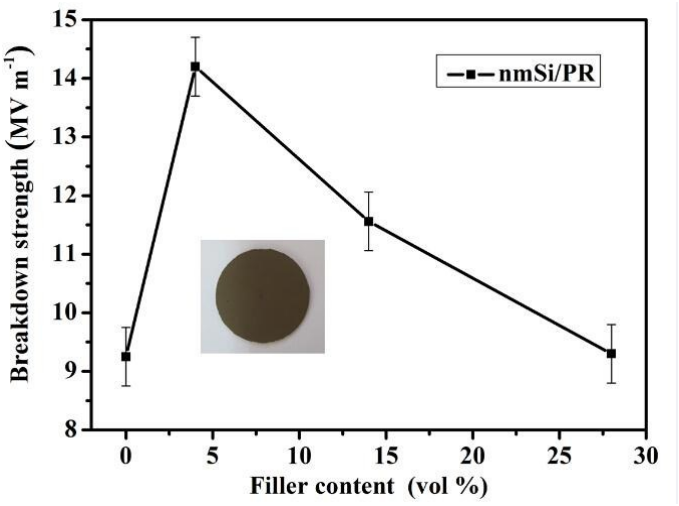

Fig. 10 Breakdown strength of Si-NS/PR composites with different volume fractions of Si-NS and digital photo of test sample (inset).

4 Conclusion

In summary, Si nanospheres with uniform size, smooth surface and good dispersity are synthesized via one-step RF thermal plasma method at atmospheric

RSC Advances Accepted Manuscript

pressure. Morphologies and size of the Si naoparticles can be adjusted by controlling experiment parameters. Formation mechanism of the Si-NSs and Si-INs is proposed based on experiment results. Furthermore, Si-NS/PR nanocomposites were prepared, and they show both high thermal conductivity and dielectric constant, which imply their potential applications in energy-storage electronic devices.

Acknowledgements

Guolin Hou and Benli Cheng contributed to the work equally and should be regarded as co-first authors.

References

1. M. Stupca, M. Alsalhi, T. Al Saud, A. Almuhanna and M. Nayfeh, *Appl. Phys. Lett.*, 2007, **91**, 063107.
2. C.-H. Lee, A. Sazonov and A. Nathan, *Appl. Phys. Lett.*, 2005, **86**, 222106.
3. C. K. Chan, R. N. Patel, M. J. O'Connell, B. A. Korgel and Y. Cui, *ACS nano*, 2010, **4**, 1443.
4. S. Sivakkumar, J. M. Ko, D. Y. Kim, B. Kim and G. Wallace, *Electrochimica Acta*, 2007, **52**, 7377.
5. Q. M. Zhang, H. F. Li, M. Poh, F. Xia, Z. Y. Cheng, H. S. Xu and C. Huang, *Nature*, 2002, **419**, 284.
6. C. W. Nan, Y. Shen and J. Ma, *Annual Review of Materials Research*, 2010, **40**, 131.
7. G. Sui, S. Jana, W. Zhong, M. Fuqua and C. Ulven, *Acta Materialia*, 2008, **56**, 2381.
8. H. Wu, A. Gu, G. Liang and L. Yuan, *J. Mater. Chem.*, 2011, **21**, 14838.
9. X. Zhang, G. Liang, J. Chang, A. Gu, L. Yuan and W. Zhang, *Carbon*, 2012, **50**, 4995.
10. B. Wang, G. Liang, Y. Jiao, A. Gu, L. Liu, L. Yuan and W. Zhang, *Carbon*, 2013, **54**, 224.
11. B. Wang, D. Qin, G. Liang, A. Gu, L. Liu and L. Yuan, *J. Phys. Chem. C*, 2013, **117**, 15487.
12. C. Wu, X. Huang, X. Wu, L. Xie, K. Yang and P. Jiang, *Nanoscale*, 2013, **5**, 3847.
13. L. Xie, X. Huang, Y. Huang, K. Yang and P. Jiang, *ACS Applied Materials & Interfaces*, 2013, **5**, 1747.
14. C. W. Beier, J. M. Sanders and R. L. Brutchey, *J. Phys. Chem. C*, 2013, **117**, 6958.
15. G. W. Lee, M. Park, J. Kim, J. I. Lee and H. G. Yoon, *Composites Part A: Applied Science and Manufacturing*, 2006, **37**, 727.
16. Y. Li, X. Huang, Z. Hu, P. Jiang, S. Li and T. Tanaka, *ACS Applied Materials & Interfaces*, 2011, **3**, 4396.
17. W. Y. Zhou, C. F. Wang, T. Ai, K. Wu, F. J. Zhao and H. Z. Gu, *Composites Part A: Applied Science and Manufacturing*, 2009, **40**, 830.
18. H. Yan, M. Zhang, C. Liu and J. Zhang, *Polymer bulletin*, 2013, **70**, 2923.
19. Z. M. Dang, L. Wang, Y. Yin, Q. Zhang and Q. Q. Lei, *Adv. Mater.*, 2007, **19**, 852.

RSC Advances Accepted Manuscript

20. I. Umezu, K. Matsumoto, M. Inada, T. Makino and A. Sugimura, *Applied Physics A*, 2004, **79**, 1545.
21. T. Müller, K. H. Heinig and W. Möller, *Appl. Phys. Lett.*, 2002, **81**, 3049.
22. K. Miura, Y. Kato, H. Hoshino and O. Hanaizumi, *Thin Solid Films*, 2008, **516**, 7732.
23. R. Amrani, D. Benlekehal, R. Baghdad, D. Senouci, A. Zeinert, K. Zellama, L. Chahed, J. Sib and Y. Bouizem, *Journal of Non-Crystalline Solids*, 2008, **354**, 2291.
24. X. Zhang, D. Neiner, S. Wang, A. Y. Louie and S. M. Kauzlarich, *Nanotechnology*, 2007, **18**, 095601.
25. Q. Cheng, S. Xu and K. K. Ostrikov, *J. Mate. Chem.*, 2009, **19**, 5134.
26. H. Zhang, M. Yao, L. Bai, W. Xiang, H. Jin, J. Li and F. Yuan, *CrystEngComm*, 2013, **15**, 1432.
27. P. Hu, L. Bai, L. Yu, J. Li, F. Yuan and Y. Chen, *Nanoscale Res. Lett.*, 2009, **4**, 1047.
28. P. Hu, F. Yuan, L. Bai, J. Li and Y. Chen, *J. Phys. Chem. C*, 2007, **111**, 194.
29. M. Yao, H. Jin, J. Li, F. Ding, C. Lu, G. Hou and F. Yuan, *Materials Letters*, 2014, **116**, 104.
30. O. Renault, R. Marlier, N. Barrett, E. Martinez, T. Baron, M. Gely and B. De Salvo, *Surf. Interface Anal.*, 2006, **38**, 486.
31. M. N. Islam, T. Ghosh, K. Chopra and H. Acharya, *Thin Solid Films*, 1996, **280**, 20.
32. S. Major, S. Kumar, M. Bhatnagar and K. Chopra, *Appl. Phys. Lett.*, 1986, **49**, 394.
33. B. Li, D. Yu and S.-L. Zhang, *Phys. Rev. B*, 1999, **59**, 1645.
34. Y. Kanemitsu, H. Uto, Y. Masumoto, T. Matsumoto, T. Futagi and H. Mimura, *Phys. Rev. B*, 1993, **48**, 2827.
35. R. P. Wang, G.W. Zhou, Y. L. Liu, S. H. Pan, H. Z. Zhang, D. P. Yu and Z. Zhang, *Physical Review B*, 2000, **61**, 16827.
36. S. Tsantilis and S. E. Pratsinis, *Langmuir*, 2004, **20**, 5933.
37. M. Shigeta and A. B. Murphy, *Journal of Physics D: Applied Physics*, 2011, **44**, 174025.
38. X. Chen and E. Pfender, *Plasma Chem. Plasma Process.*, 1982, **2**, 185.
39. Y. Lee, Y. Chyou and E. Pfender, *Plasma Chem. Plasma Process.*, 1985, **5**, 391.
40. D. Bernardi, V. Colombo, E. Ghedini and A. Mentrelli, *The European Physical Journal D: Atomic, Molecular, Optical and Plasma Physics*, 2003, **22**, 119.
41. H. Lindner, A. Murtazin, S. Groh, K. Niemax and A. Bogaerts, *Analytical chemistry*, 2011, **83**, 9260.
42. Y. Wan, V. Prasad, G. X. Wang, S. Sampath and J. Fincke, *Journal of heat transfer*, 1999, **121**, 691.
43. N. Petermann, N. Stein, G. Schierning, R. Theissmann, B. Stoib, M. S. Brandt, C. Hecht, C. Schulz and H. Wiggers, *Journal of Physics D: Applied Physics*, 2011, **44**, 174034.
44. H. B. Gu, S. Tadakamalla, Y. D. Huang, H. A. Coloradc, Z. P. Luo, N. Haldolaarachchige, D. P. Young, S. Y. Wei and Z. H. Guo, *Acs Applied Materials & Interfaces*, 2012, **4**, 5613.
45. L. S. Schadler, S. K. Kumar, B. C. Benicewicz, S. L. Lewis and S. E. Harton, *Mrs Bulletin*, 2007, **32**, 335.
46. C. P. R. Nair, R. L. Bindu and K. N. Ninan, *Polymer Degradation and Stability*, 2001, **73**, 251.
47. J. G. Wang, H. Y. Jiang and N. Jiang, *Thermochim. Acta*, 2009, **496**, 136.
48. Y. F. Chen, Z. Q. Chen, S. Y. Xiao and H. B. Liu, *Thermochim. Acta*, 2008, **476**, 39.
49. H. B. Gu, S. Tadakamalla, X. Zhang, Y. D. Huang, Y. Jiang, H. A. Colorado, Z. P. Luo, S. Y. Wei and Z. H. Guo, *Journal of Materials Chemistry C*, 2013, **1**, 729.
50. Y. Chen, J. Tao, S. Li and N. M. Khashab, *Acs Applied Materials & Interfaces*, 2014, **6**, 9013.

RSC Advances Accepted Manuscript

51. K. S. Khare, F. Khabaz and R. Khare, *Acs Applied Materials & Interfaces*, 2014, **6**, 6098.
52. S. Wang, M. Tambraparni, J. Qiu, J. Tipton and D. Dean, *Macromolecules*, 2009, **42**, 5251.
53. F. Yavari, H. R. Fard, K. Pashayi, M. A. Rafiee, A. Zamiri, Z. Yu, R. Ozisik, T. Borca-Tasciuc and N. Koratkar, *J. Phys. Chem. C*, 2011, **115**, 8753.
54. R. Kochetov, A. Korobko, T. Andritsch, P. Morshuis, S. Picken and J. Smit, *Journal of Physics D: Applied Physics*, 2011, **44**, 395401.
55. D. Stauffer and A. Aharony, *Introduction to percolation theory*, Taylor and Francis, 1991.
56. A. Jonscher, Electrical Insulation and Dielectric Phenomena, *Annual Report.*, Conference on, 1990.
57. X. Huang, C. Zhi, P. Jiang, D. Golberg, Y. Bando and T. Tanaka, *Nanotechnology*, 2012, **23**, 455705.
58. B. Chu, X. Zhou, K. Ren, B. Neese, M. Lin, Q. Wang, F. Bauer and Q. Zhang, *Science*, 2006, **313**, 334.
59. P. Hu, Y. Song, H. Liu, Y. Shen, Y. Lin and C. W. Nan, *J. Mater. Chem. A*, 2013, **1**, 1688.
60. S. P. Fillery, H. Koerner, L. Drummy, E. Dunkerley, M. F. Durstock, D. F. Schmidt and R. A. Vaia, *ACS Applied Materials & Interfaces*, 2012, **4**, 1388.
61. J. K. Nelson and J. C. Fothergill, *Nanotechnology*, 2004, **15**, 586.
62. L. Flandin, L. Vouyovitch, A. Beroual, J. L. Bessède and N. Alberola, *Journal of Physics D: Applied Physics*, 2005, **38**, 144.

RSC Advances Accepted Manuscript

For Table of Contents Use Only

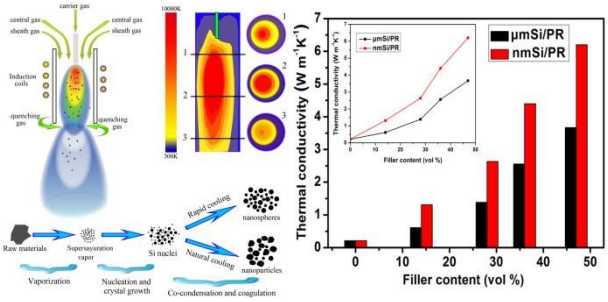

Nanocomposites with high thermal conductivity and large dielectric constant incorporated with Si nanospheres prepared by thermal plasma are reported.

RSC Advances Accepted Manuscript